The Astrophysical Journal, 958:177 (10pp), 2023 December 1 https://doi.org/10.3847/1538-4357/ad0296

Broadband X-Ray Timing and Spectral Characteristics of the Accretion-powered Millisecond X-Ray Pulsar MAXIJ1816-195

Zhaosheng Li[1], Lucien Kuiper[2], Mingyu Ge[3], Maurizio Falanga[4,5], Juri Poutanen[6], Long Ji[7], Yuanyue Pan[1], Yue Huang[3], Renxin Xu[8,9], Liming Song[3], Jinlu Qu[3], Shu Zhang[3], Fangjun Lu[3], and Shuang-Nan Zhang[3]
[1] Key Laboratory of Stars and Interstellar Medium, Xiangtan University, Xiangtan 411105, Hunan, People's Republic of China; lizhaosheng@xtu.edu.cn
[2] SRON-Netherlands Institute for Space Research, Niels Bohrweg 4, 2333 CA, Leiden, The Netherlands
[3] Key Laboratory of Particle Astrophysics, Institute of High Energy Physics, Chinese Academy of Sciences, 19B Yuquan Road, Beijing 100049, People's Republic of China; gemy@ihep.ac.cn
[4] International Space Science Institute (ISSI), Hallerstrasse 6, 3012 Bern, Switzerland
[5] Physikalisches Institut, University of Bern, Sidlerstrasse 5, 3012 Bern, Switzerland
[6] Department of Physics and Astronomy, University of Turku, FI-20014, Finland
[7] School of Physics and Astronomy, Sun Yat-sen University, Zhuhai 519082, People's Republic of China
[8] Department of Astronomy, School of Physics, Peking University, Beijing 100871, People's Republic of China
[9] Kavli Institute for Astronomy and Astrophysics, Peking University, Beijing 100871, People's Republic of China
Received 2023 March 21; revised 2023 October 6; accepted 2023 October 10; published 2023 November 24

Abstract

We studied the broadband X-ray timing and spectral behaviors of the newly confirmed accreting millisecond X-ray pulsar MAXI J1816−195 during its 2022 outburst. We used data from the Insight-HXMT Medium Energy (ME) and High Energy (HE) telescopes, NICER, and NuSTAR that cover the energy range between 0.8 and 210 keV. A coherent timing analysis of solely the Insight-HXMT HE data across the full outburst revealed a complex behavior of the timing residuals, also prominently visible in the independent Insight-HXMT ME and NICER data, particularly at the rising part of the outburst and at the very end in the NICER data. Therefore, we broke down the full outburst into a (noisy) rising part, covering only about five days, from MJD 59737.0 to 59741.9, and a decaying part, lasting for 19 days across MJD 59741.9–59760.6. Fitting for the decaying part, a timing model including a frequency ν and frequency time derivative $\dot{\nu}$ component yielded a value of $(+9.0 \pm 2.1) \times 10^{-14}$ Hz s^{-1} for $\dot{\nu}$, which could be interpreted as a spinup under our model assumptions. We detected X-ray pulsations up to ∼95 keV in a combination of Insight-HXMT HE observations. The pulse profiles were quite stable over the whole outburst and could be well described by a truncated Fourier series using two harmonics, the fundamental and the first overtone. Both components kept alignment in the range 0.8–64 keV. The joint and time-averaged NICER and Insight-HXMT spectra in the energy range 1–150 keV were well fitted by the absorbed Comptonization model `compps` plus disk blackbody with two additional Gaussian components. Using the bolometric flux and spinup values both evaluated during the decay phase, we determined a magnetic field strength of (0.2–2) $\times 10^8$ G for MAXI J1816−195.

Unified Astronomy Thesaurus concepts: Neutron stars (1108); Millisecond pulsars (1062)

1. Introduction

As a subclass of neutron star (NS) low-mass X-ray binary, accreting millisecond X-ray pulsars (AMXPs) are usually confirmed by their coherent pulsations during outburst, with spin periods of a few milliseconds and orbital periods between 40 minutes and 5 hr, based on the current sample (see Campana & Di Salvo 2018; Papitto et al. 2020; Patruno & Watts 2021; Di Salvo & Sanna 2022 for reviews). The recycling scenario suggested that AMXPs are progenitors of (radio) millisecond pulsars (Alpar et al. 1982; Radhakrishnan & Srinivasan 1982). This picture has been verified by the discoveries of AMXPs, starting with SAX J1808.4–3658 by RXTE (Wijnands & van der Klis 1998), the discovery of the pulsar spinup induced by accretion (Falanga et al. 2005b), and by swinging between accretion- and rotation-powered states in IGR J18245–2452 (Papitto et al. 2013).

The new X-ray transient MAXI J1816−195 was discovered by MAXI/Gas Slit Camera on 2022 June 7 during its outburst that year (Negoro et al. 2022). Using the Swift localization, NICER detected pulsations and thermonuclear type I X-ray bursts from MAXI J1816−195, confirming that the source is an AMXP with a spin frequency of 528 Hz, an orbital period of 4.83 hr, and a projected semimajor axis of 0.26 lt-s (Bult et al. 2022a, 2022b, 2022c; Kennea et al. 2022). The mass of the companion star was determined to be in the range 0.10–0.55 $M_\odot$ (Bult et al. 2022a). Meanwhile, Insight-HXMT found X-ray pulsations from MAXI J1816−195 in the hard X-ray/soft γ-ray band (Li et al. 2022). Bult et al. (2022a) proposed the flux bias model, which accounts for the effects of the accretion torque and/or the wandering of the hotspot on the NS surface, to explain the structures left in the timing residuals across the outburst. Chen et al. (2022) reported the detection of 73 type I X-ray bursts by Insight-HXMT from MAXI J1816−195 and obtained an upper limit of the distance as 6.3 kpc. P. Wang et al. (2023, in preparation) found the type I X-ray bursts rate to decrease for bolometric flux higher than $\sim 1.04 \times 10^{-8}$ erg cm^{-2} s^{-1} and estimated the distance to the source at ∼3.4 kpc (Cavecchi et al. 2020).

Since the onset of the 2022 outburst, a search for radio, optical, and near-infrared emission from MAXI J1816−195 had been carried out. The radio emission of MAXI J1816−195

showed significant evolution: at 1.28 GHz, with a flux density of 4.2 ± 0.4 mJy on 2022 June 9 and a 3σ upper limit of 70 μJy on 2022 June 11 by MeerKAT; at 5.5 GHz, with a flux density of 135 ± 35 μJy on 2022 June 12 by the Australia Telescope Compact Array; and at 6 GHz, with a flux density of 457 ± 20 μJy on 2022 June 18 by the Very Large Array (VLA; Beauchamp et al. 2022; Bright et al. 2022). However, radio pulsations were not detected. The likely optical and near-infrared counterpart of MAXI J1816−195 had been identified (de Martino et al. 2022; Kong 2022). When MAXI J1816−195 evolved toward the quiescent state about one month after the start of the outburst, X-ray emission from a dust-scattered halo around the source position was detected by Swift (Beardmore et al. 2022).

In this work, we present a broadband timing and spectral analysis of MAXI J1816−195. We introduce the instruments—Insight-HXMT, NICER, and NuSTAR—and the performed observations in Section 2. The timing and the broadband spectral results are reported in Sections 3 and 4, respectively, and our findings are discussed in Section 5.

2. Observations and Data Reduction

We analyzed the data from MAXI J1816−195 collected by Insight-HXMT, NICER, and NuSTAR.

2.1. Insight-HXMT

Insight-HXMT (Insight Hard X-ray Modulation Telescope; Zhang et al. 2020) is the first Chinese X-ray telescope, and it is equipped with three slat-collimated instruments: the Low Energy X-ray telescope (1–12 keV; Chen et al. 2020), the Medium Energy X-ray telescope (ME; 5–35 keV; Cao et al. 2020), and the High Energy X-ray telescope (HE; 20–350 keV; Liu et al. 2020), providing capabilities for broadband X-ray timing and spectroscopy. Insight-HXMT carried out high-cadence observations of MAXI J1816−195 starting on MJD 59738.17, ∼0.5 days after the detection by MAXI. The set of 79 ME and 77 HE observations includes runs P0404275001–P0404275024. The HE and ME data were studied to investigate the timing and spectral properties of the source because of their broadband X-ray coverage and good time resolution (∼2 μs for HE, ∼20 μs for ME). We analyzed the data using the Insight-HXMT Data Analysis Software, version 2.05. The ME and HE data were calibrated by using the scripts `mepical` and `hepical`, respectively. The good time intervals were individually selected from the scripts `megtigen` and `hegtigen` with the standard criteria, that is, ELV > 0, the satellite located outside the South Atlantic Anomaly region, and the offset angle from the pointing direction being smaller than $0\farcm04$. In total, 73 type I X-ray bursts have been observed by ME (Chen et al. 2022), which were removed in the timing and spectral analysis. No bursts were found in HE, because the burst spectra are usually soft. Background-subtracted light curves for ME and HE were generated (see Figure 1). The outburst light curve of Insight-HXMT ME showed a fast rise during the early days of the outburst and a slow decay in the next 25 days. However, the Insight-HXMT HE light curve for the 20–50 keV band dropped continuously from ∼100 cts s^{-1} since the start of the observations to the quiescent level during the outburst. The spectra and their response matrix files are produced by the tools `hespecgen` and `herspgen` for HE and `mespecgen` and `merspgen` for ME, respectively.

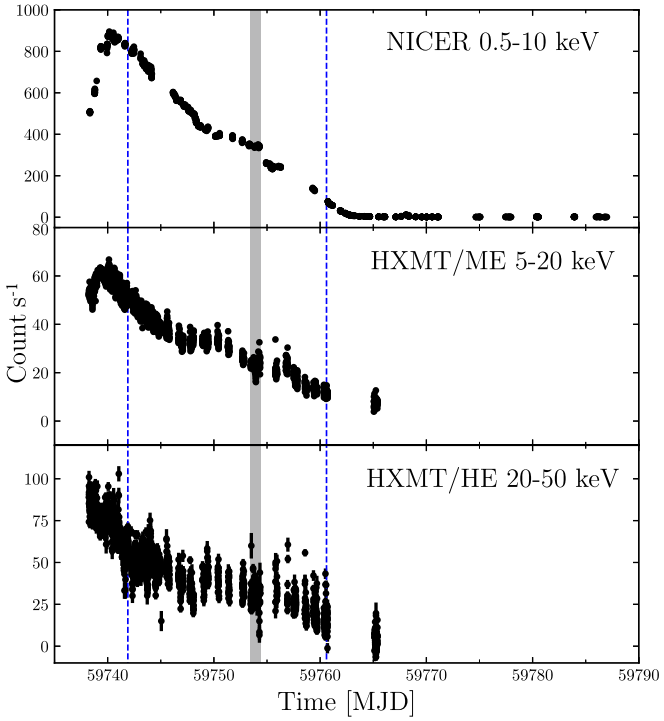

Figure 1. The light curves of MAXI J1816−195 during its 2022 outburst. From top to bottom: the 100 s binned light curves from NICER, Insight-HXMT ME, and Insight-HXMT HE are displayed, respectively. The energy range of each light curve is indicated in each panel. The gray area marks the time of NuSTAR observation. Time intervals covering X-ray bursts are removed. The blue dashed lines represent the time interval that we used for the derivation of our timing models; see Table 1 and Section 3.

Finally, we obtained the cleaned events using `mescreen` and `hescreen` and barycentered with the tool `hxbary`.

2.2. NICER

NICER started regular observations of MAXI J1816−195 on 2022 June 7 (MJD 59737.6; obs. ID 5202820101), several hours after the detection by MAXI, and ended these on 2022 August 3 (MJD 59794.01; obs. ID 5533013504), when the source was already several weeks into its quiescent state. We performed the standard data processing using the NICER Data Analysis Software. The default filtering criteria were applied to extract the cleaned event data. Next, we extracted 1 s light curves by using `xselect` for the 0.5–10 and 12–15 keV bands to search for type I X-ray bursts and flaring background, respectively. Time intervals containing X-ray bursts or background flares were removed in further analysis. The 0.5–10 keV light curve showed a profile similar to Insight-HXMT ME, i.e., a fast rise in the first few days and a decay to the quiescent level during the next ∼25 days (see the top panel of Figure 1).

The background spectra were produced from the `nibackgen3C50` tool (Remillard et al. 2022). The redistribution matrix file and ancillary response file were generated from the tools `nicerarf` and `nicerrmf`, respectively.

In the pulse profile analysis of the NICER data (see Section 3.2), we used obs. IDs 5533013001–5533013502 (MJD 59769.566–59786.993; cleaned exposure time 14.388 ks), performed when the source had already reached its quiescent state with undetectable (pulsed) flux levels, for the estimation

of the local background to obtain background-corrected fractional amplitudes.

2.3. NuSTAR

NuSTAR observed MAXI J1816−195 on 2022 June 23 (obs. ID 90801315001; MJD ∼59753.456 − 59754.413) for about 35.7 ks. We cleaned the event file using the NuSTAR pipeline tool `nupipeline` for both FPMA and FPMB. The light curves and spectra were extracted from a circular region with a radius of 100″ centered on the source location by using `nuproducts`, and the response and ancillary response files were produced simultaneously. To extract the background spectra, we chose a source-free circular background region centered at $(\alpha_{2000}, \delta_{2000}) = (18^{h}16^{m}28\overset{s}{.}4048, -19°39'56\overset{''}{.}308)$ with a radial aperture of 100″. From the light curves, four type I X-ray bursts were identified (see also Mandal et al. 2023). For the timing and spectral analysis, the time intervals during these bursts are discarded, resulting in a total exposure time of 29.6 ks.

In the timing analysis, we barycentered event data from the source region, adopting a 90″ extraction radius, using `HEASOFT` multimission tool `barycorr v2.16`, with NuSTAR fine-clock-correction file #142, yielding time tags accurate at the 60–100 μs level (Bachetti et al. 2021) in absolute time. To obtain background-corrected timing characteristics, such as fractional amplitudes, we used the above-mentioned background region, but now with a 90″ extraction radius.

3. Timing Analysis

Irrespective of the instrument, in the timing analyses we converted the Terrestrial Time arrival times of the selected events to arrival times at the solar system barycenter (on a Barycentric Dynamical Time (TDB) timescale). For this process, throughout in this work we used: (1) the JPL DE405 solar system ephemeris; (2) the instantaneous spacecraft position with respect to the Earth's center; and (3) the (most accurate) VLA position of MAXI J1816−195, $\alpha_{2000} = 18^{h}16^{m}52\overset{s}{.}41168$ and $\delta_{2000} = -19°37'57\overset{''}{.}40138$ (Beauchamp et al. 2022), which differ by 0″.4 in decl. from the Swift location (Kennea et al. 2022). Moreover, in the selection procedures, we ignored time intervals during which type I X-ray bursts or high background flaring occurred.

3.1. Insight-HXMT and NICER Timing Analysis

Initially, we constrained the timing analysis to Insight-HXMT HE data using only events with measured energies between 20 and 35 keV. Before generating phase-coherent timing models (ephemerides) describing accurately the spin frequency evolution across the outburst, we first need to correct the barycentered event arrival times for the periodic orbital motion effects. Early mission data covering only a part (MJD 59738–59752) of the full data set available for Insight-HXMT HE analysis had been used to improve the orbital parameters of MAXI J1816−195, applying an optimization scheme based on a SIMPLEX algorithm (see De Falco et al. 2017a; Li et al. 2021 for more details) by iteratively improving the $Z_2^2(\phi)$-test statistics (Buccheri et al. 1983) with respect to the pulse frequency ν, the orbital period $P_{\rm orb}$, and time of the ascending node $T_{\rm asc}$. The optimized values for the (most critical) orbital parameters $P_{\rm orb}$ and $T_{\rm asc}$, while fixing the eccentricity to zero and the projected semimajor axis $a_{\rm x} \sin i$ to the value quoted in Bult et al. (2022b), are listed in Table 1. The obtained values are fully consistent within 1σ with the best orbital parameters obtained later by Bult et al. (2022a) using the full NICER database. Therefore, we kept the values for the orbital parameters as derived from our three-parameter optimization scheme using 20–35 keV Insight-HXMT HE data.

Table 1
Positional, Orbital, and Spin Parameters Derived in This Work and Used as Fixed Values from Literature for MAXI J1816−195

Parameter	Values	Units
α_{2000}	$18^{h}16^{m}52\overset{s}{.}41168(12)$	…
δ_{2000}	$-19°37'57\overset{''}{.}40138(473)$	…
JPL Ephemeris	DE405	…
$P_{\rm orb}$	17402.5786(60)	s
$a_{\rm x} \sin i$	0.262 948(18)	lt-s
e	0 (fixed)	…
$T_{\rm asc}$	59738.875 632(4)	MJD (TDB)
Constant Frequency Model		
Validity range	59741.9 − 59760.6	MJD (TDB)
t_0 (Epoch)	59741.0	MJD (TDB)
ν	528.611 105 832(4)	Hz
χ^2/d.o.f	86.78/(47 − 1) = 1.886	…
Quadratic / Spinup Model		
Validity range	59741.9 − 59760.6	MJD (TDB)
t_0 (Epoch)	59741.0	MJD (TDB)
ν	528.611 105 774(12)	Hz
$\dot{\nu}$	$(9.0 \pm 2.1) \times 10^{-14}$	Hz s^{-1}
χ^2/d.o.f	68.18/(47 − 2) = 1.515	…

After correcting for the orbital motion effects, we performed a time-of-arrival (ToA; see Kuiper & Hermsen 2009 for more details) analysis to obtain accurate estimates for the pulse frequency ν and (if required) its first time derivative $\dot{\nu}$ over a certain time interval. We obtained 69 ToAs for Insight-HXMT HE (20–35 keV) covering MJD 59738–59761. Similar analyses yielded 73 ToAs for Insight-HXMT ME, restricted to the 10–20 keV band (MJD 59738–59761), and 26 ToAs for NICER using 1.8–10 keV events across MJD 59737–59761.

Fitting the complete Insight-HXMT HE ToA data set with a constant frequency model resulted in a very poor fit with an unacceptable χ^2. Ignoring 22 ToAs from the first ∼5 days of the outburst yielded reasonable fits, assuming a constant frequency model and a model including a frequency derivative term. Both are listed in Table 1. The constant frequency model is fully consistent at 1σ confidence with the corresponding model, based solely on NICER data, shown in Table 1 of Bult et al. (2022a) for 46 degrees of freedom (dof).

The model with both the ν and $\dot{\nu}$ terms, however, improves upon the constant frequency model by reducing the χ^2 from 86.78 to 68.18, adding one fit parameter. Applying a maximum likelihood ratio test to assess the model improvement yields an improvement of $(86.78 - 68.18)^{0.5} = 4.3\sigma$, adopting one dof (= the additional fit parameter).[10] The measured $\dot{\nu}$ of $(9.0 \pm 2.1) \times 10^{-14}$ Hz s^{-1} can be interpreted as a spinup across the time interval MJD 59741.9–59760.6. We have also investigated the effects of employing a flux bias model in the ToA fit

[10] The square root relation holds only for the case of one additional fit parameter (= one dof).

procedure, by adding a (flux) bias term in the form, $\Phi_{\rm bias} = \alpha(C/C_{\rm max})^{\Gamma}$ with $C_{\rm max} = 895.37$ c s^{-1} (the maximum observed count rate in the 0.5–10 keV NICER bandpass) to the pulse-phase residual relation in analogy with Bult et al. (2022a; see their Equation (1)). Note that in Table 1 of Bult et al. (2022a), both optimized flux bias model parameters, their b and Γ, are listed abusively with a plus sign. Taking this sign inconsistency into account, we could reproduce their findings and obtained $\Gamma = -1.05 \pm 0.15$, consistent within 1σ confidence with their value of -1.20 ± 0.20, employing the *full* NICER ToA data set running from MJD 59737.748–59762.610. Constraining the NICER ToA data set to MJD 59742.370–59762.610, and so ignoring the rising and maximum part of the light curve (see Figure 1), we obtained a flux bias index of $\Gamma = -0.77 \pm 0.09$, but as with the full-range NICER model shown before, with a statistically unacceptable fit quality of $\chi^2_r \sim 3.54$ compatible with the results shown in Bult et al. (2022a). Next, we fitted a constant frequency plus flux bias model with a *fixed* index $\Gamma = -0.77$ to the Insight-HXMT-HE ToA data set covering MJD 59741.9–59760.6, the decaying part of the outburst. This model improves upon the constant frequency model by reducing the χ^2 from 86.78 to 83.10, adding one free parameter (the flux bias model scale α), which represents an $(86.78 - 83.10)^{0.5} = 1.92\sigma$ improvement with respect to the constant frequency model, applying a maximum likelihood ratio test. The best-fit flux bias scale parameter is $\alpha = (-7.1 \pm 3.7) \times 10^{-3}$, while $\nu = 528.611\,105\,851(11)$ Hz. Therefore, the spinup model for the decaying part of the outburst (covering MJD 59741.9–59760.6) provides a better data description than the flux bias model for the Insight-HXMT-HE ToA data set.

The pulse-phase residuals of the complete sets of ToAs from all three instruments combined (each determined for a different energy band) after folding upon the (Insight-HXMT HE 20–35 keV–based) spinup model are shown in Figure 2. Irrespective of the energy band, each instrument showed a quite similar behavior: during the first ∼5 days of the outburst —the rising flux part—there is a structured residual feature that can be described by a (short-duration) spindown model. This feature is the cause of the very poor χ^2 when the full ToA data sets are considered (see also Table 1 of Bult et al. 2022a, indicating unacceptable χ^2 fit values). Also, the steep positive excursions for the NICER ToAs at the early beginning and very end (not covered by Insight-HXMT observations) of the outburst are striking in Figure 2. It is clear that even a (bolometric) flux bias model as well as the constant frequency and quadratic models considered in this work cannot describe the *full* set of residuals, consistent with Bult et al. (2022a).

3.2. Pulse Profile Analysis

With the accurate orbital and (spinup) timing models (see Table 1), we converted the event arrival times from each high-energy instrument to pulse phases. To obtain high-statistics pulse-phase distributions (pulse profiles including background), we combined the phase information for each instrument across the validity interval (MJD 59741.9–59760.9) and sorted these on (measured) energy. We verified for each instrument that the pulse shape for each individual observation constituting the combination remained the same within statistical uncertainties. The measured pulse-phase distributions for the four different high-energy instruments are shown in Figure 3 for various different energy bands covering the 0.8–210 keV range.

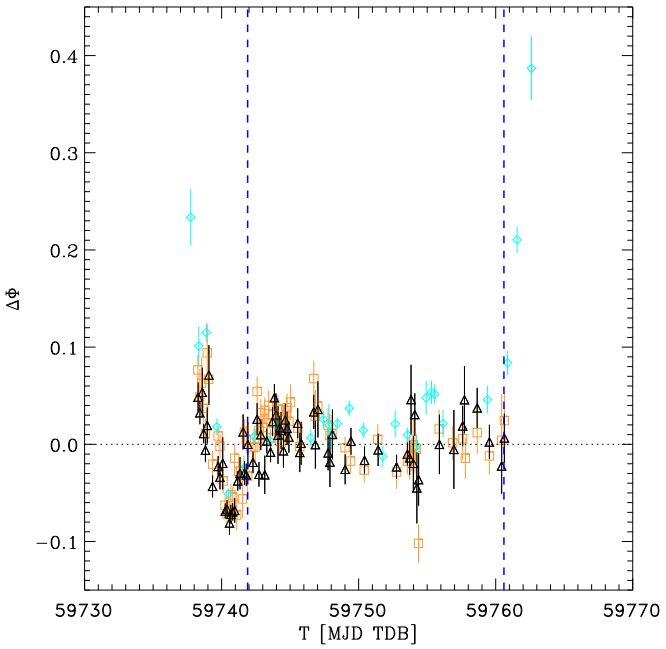

Figure 2. Pulse-phase residuals of Insight-HXMT HE (open black triangles; 20–35 keV), Insight-HXMT ME (open orange squares; 10–20 keV), and NICER (open aqua diamonds; 1.8–10 keV) ToAs with respect to a two-parameter timing model (including a quadratic/spinup term) valid for the range MJD 59741.9–59760.6. These models are based on solely Insight-HXMT HE ToAs (black data points). The interval bounded by the two blue dashed lines represents this time interval that has been used to derive the timing models given in Table 1. Note that there are no ToA measurements beyond MJD 59760.6 for Insight-HXMT HE (and ME), contrary to NICER.

Panels (a)–(c) of Figure 3 show the NICER pulse profiles for the energy intervals 0.8–1.8, 1.8–3, and 3–10 keV, respectively, while panels (d)–(f) show the Insight-HXMT ME profiles for the 5–10, 10–20, and 20–35 keV bands. The NuSTAR profiles are displayed in panels (g)–(k), covering the 3–79 keV energy range. Noteworthy is that comparing the NICER and NuSTAR 3–10 keV distributions, shown in panels (c) and (g), respectively, a small phase shift of 0.065 ± 0.020 is detectable, which is just compatible with the absolute timing accuracy of NuSTAR (Bachetti et al. 2021). Pulsed emission is detected significantly up to ∼60 keV, with a nonuniformity significance of 5.4σ for the 35–60 keV band (panel (j)), adopting a Z^2_2-test (Buccheri et al. 1983). This test applied to the 60–79 keV band (panel (k)) yielded an insignificant result of 1.3σ. Finally, panels (l)–(p) show the Insight-HXMT HE profiles for energies of 20–30, 30–50, 50–65, 65–95, and 95–210 keV, respectively. Interestingly, pulsed emission is detected significantly up to ∼95 keV. The 65–95 keV band (panel (o)) shows a nonuniform significance of 4.4σ, applying a Z^2_2-test with indications for a second weaker pulse near phase 0.15 that seems to pop up at energies above ∼50 keV (panels (n)–(o)). The nonuniformity significance for the distribution shown in panel (p) for the 95–210 keV band is about 1.1σ and so is insignificant.

To obtain quantitative information about the morphology changes of the pulse profiles as a function of energy, we fit the pulse profiles with a truncated Fourier series given by a formula

$$F(\phi) = A_0 + \sum_{k=1}^{2} A_k \cos[2\pi\, k(\phi - \phi_k)], \qquad (1)$$

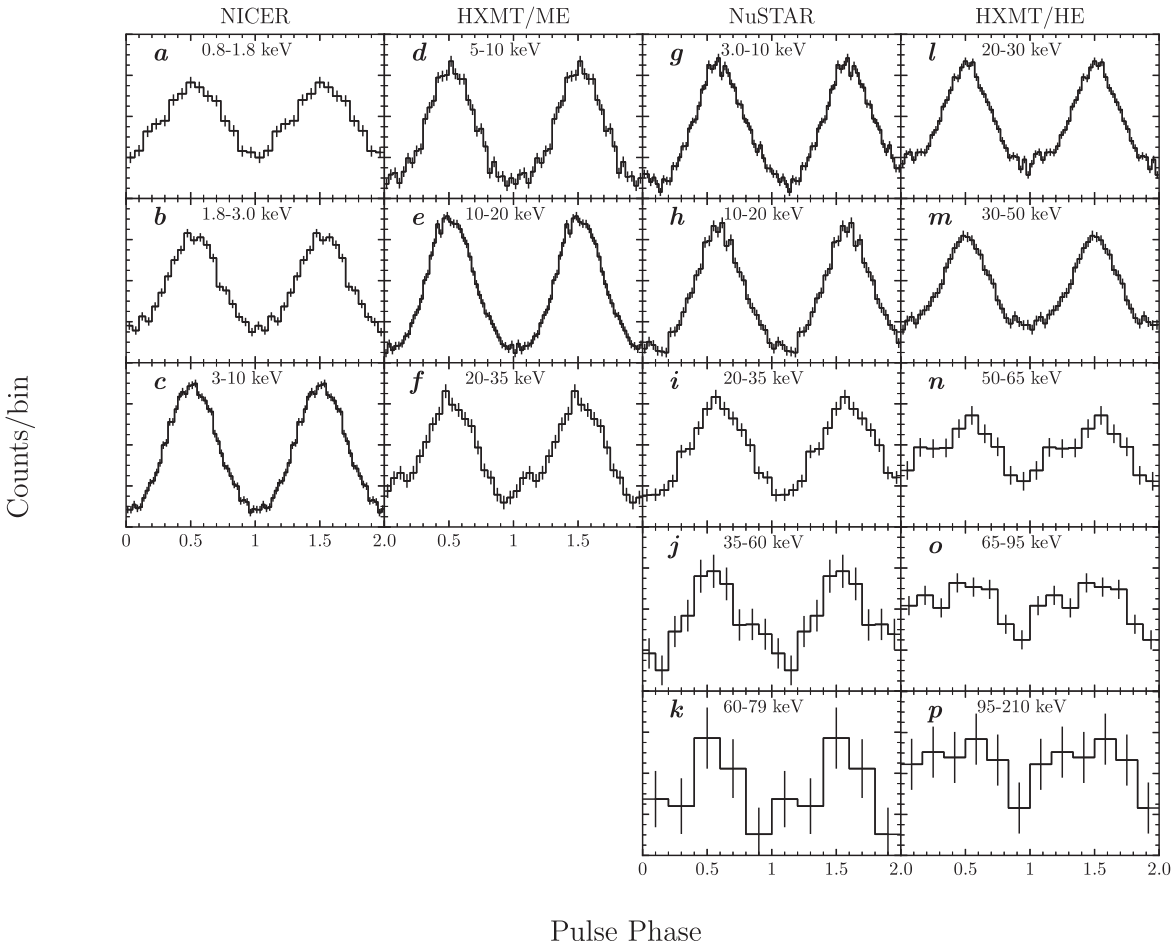

Figure 3. The 0.8–210 keV broadband pulse-phase distributions of MAXI J1816−195 observed by NICER (panels (a)–(c); 0.8–10 keV), NuSTAR (panels (g)–(k); 3–79 keV), and Insight-HXMT (panels (d)–(f); 5–35 keV for ME; and panels (l)–(p); 20–210 keV for HE). In order to improve clarity, two cycles are shown. The error bars represent 1σ errors. The morphology is almost unchanged with energy. All profiles reach their maximum near phase ∼0.5.

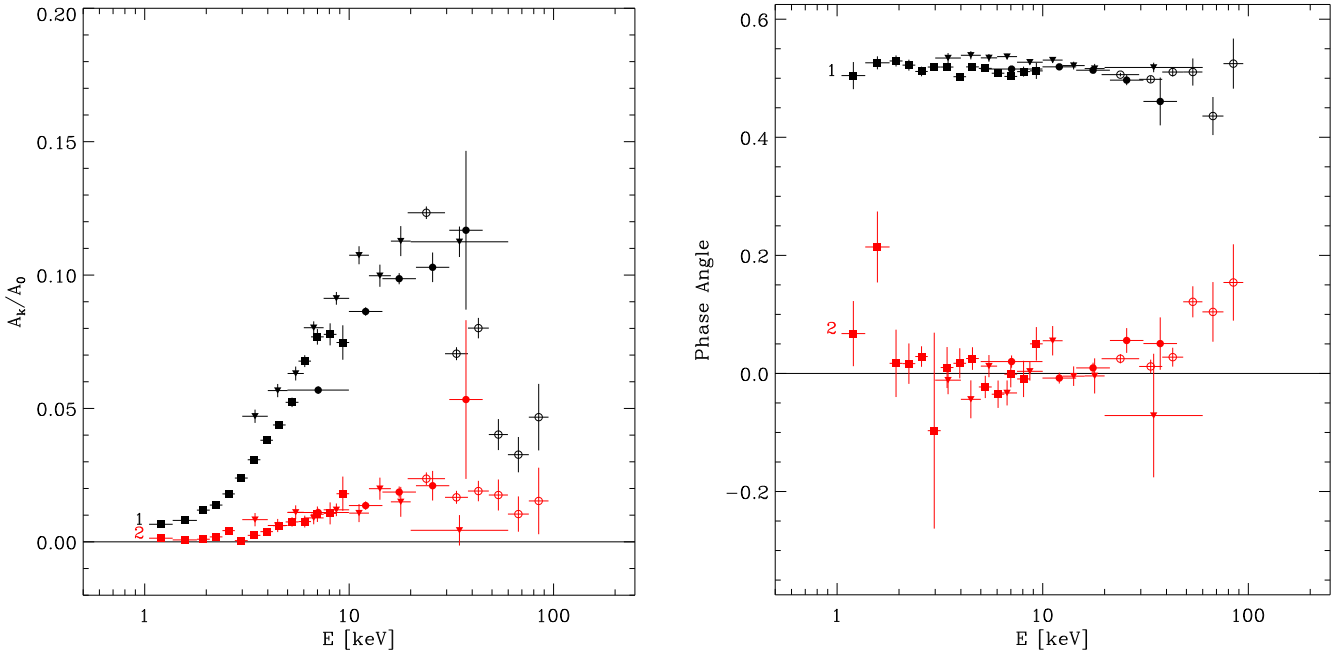

Figure 4. Left: the fractional amplitude of various harmonics: (1) fundamental overtone (black crosses) and (2) first overtone (red crosses) as a function of energy using background-corrected data from NICER (filled squares), NuSTAR (triangles), Insight-HXMT ME (filled circles), and Insight-HXMT HE (open circles). Right: the phase angle (in units of radians/2π) as a function of energy for the two Fourier components, the fundamental (in black) and the first overtone (in red), which are independent of the background-subtraction method.

where A_1 and A_2 are the amplitudes, ϕ_1 and ϕ_2 are the phase angles (in radians/2π) of the fundamental and the first overtone, respectively, and A_0 is the constant level of the profile. We verified that higher harmonics are not required to accurately describe the data. The left panel of Figure 4 shows the background-corrected fractional amplitudes A_k/A_0 of the fundamental (black) and first overtone (red) for all four instruments covering the 0.8–95 keV band, across which we detected significant pulsed emission.

The background correction determination was straightforward for NICER and NuSTAR. We used for the former nonimaging instrument the data from observations when the source was completely Off (see Section 2.2), with a combined Good Time Interval (GTI) exposure of 14.388 ks. Along with the On-time GTI exposure of 51.735 ks, this yielded a scale factor $s_{\rm bg}$ of 3.5957 to be applied in the background subtraction. For the latter (imaging) instrument, data from a different source-free location in the field of view with equal area as the source region ($s_{\rm bg} \equiv 1.0$) were used.

For the nonimaging Insight-HXMT ME/HE (with GTI exposures of 186.171 and 132.093 ks, respectively, for the validity interval during the On source period), the last observations of MAXI J1816−195 performed on MJD 59765 (2022 July 5) totaling exposure times of 13.474 ks and 9.022 ks for ME and HE, respectively, were used to estimate the underlying background, when the source did not show pulsed emission anymore, but was not completely Off (see, e.g., Beardmore et al. 2022, who reported the detection of the source at a 4.1σ level in 5.2 ks Swift X-Ray Telescope (XRT) data taken a day later on MJD 59766).

Thus, the ME/HE event data of MJD 59765 still contain a tiny contribution from MAXI J1816−195, which would yield an oversubtraction when applied uncorrected in the background-subtraction procedure. Demanding that the background subtraction did not yield a negative value for energy bands at the high end of the sensitivity window of both instruments (ME $\gtrsim$30 keV; HE $\gtrsim$95 keV), we could estimate the genuine background contribution in both samples. For the ME/HE, we found that ∼9% and ∼5% of the events from the background sample were originating from the "almost" Off MAXI J1816−195, respectively. Taking these fractions into account in the background-subtraction process showed that the A_1/A_0 (and also the A_2/A_0) values obtained for ME/HE matched with NuSTAR values obtained in the overlapping energy range.

It is clear from the left panel of Figure 3 that the pulsed fraction of the fundamental (black) overtone gradually increases with energy from ∼0.5% to 10%–12%, going from ∼0.8 to ∼10 keV, where a plateau is reached. Above ∼35 keV, a decrease sets in, to values of 3%–5% above 50 keV. The first overtone (red) saturates at $\gtrsim$10 keV to a ∼2% value, without a clear decrease beyond. This means that the A_2/A_1 ratio increases the higher the energy, implying that the first overtone contributes more significantly at higher energies.

The right panel of Figure 3 shows the phases of the maxima of the fundamental (black) and first overtone (red) for the four instruments, specifying the alignment of the components constituting the pulse profile. It is noteworthy that these quantities, ϕ_1 and ϕ_2, are independent of the used background method.

For NuSTAR, which provided a snapshot during the full outburst, we have subtracted 0.065 (in phase units)—still within its absolute timing accuracy—from the measured ϕ_1 and ϕ_2 values for alignment purposes with NICER. It is clear that, irrespective of the instrument, both quantities are stable within statistical uncertainties until ∼50 keV, beyond which the first overtone moves closer to the fundamental overtone. Combined with the increase of the A_2/A_1 ratio at those energies, this means that a second bump/maximum in the pulse profile in front of the main maximum becomes more prominent at $\gtrsim$50 keV energies.

4. Spectral Analysis

The spectral analysis was carried out using XSPEC, version 12.12.1 (Arnaud 1996). We first performed the joint spectral evolution analysis for NICER and Insight-HXMT observations (Section 4.1), and then we studied the quasi-simultaneous broadband spectra of NICER, NuSTAR, and Insight-HXMT (Section 4.2). All spectra are grouped by the tool `ftgrouppha`. For NICER and NuSTAR spectra, we applied the optimal binning method (Kaastra & Bleeker 2016). The Insight-HXMT spectra were grouped with a minimal signal-to-noise ratio of 3 related to their backgrounds. All uncertainties of the spectral parameters are provided at a 1σ confidence level for a single parameter.

4.1. The Spectral Evolution of Joint NICER and Insight-HXMT Observations

There were many quasi-simultaneous NICER and Insight-HXMT observations of MAXI J1816−195, which allow us to perform a detailed broadband spectral analysis for the whole outburst. We found that each NICER observation in the MJD 59738–59761 range can be (partially) covered by one to six Insight-HXMT observations. We combined the Insight-HXMT spectra and then carried out joint NICER and Insight-HXMT spectral fitting. We adopted the energy ranges of 1–10 keV for NICER spectra, 10–35 keV for Insight-HXMT ME, and 25–150 keV for Insight-HXMT HE. We fit all the spectra by using a combination of the thermal Comptonization model, `compps`, in the slab geometry (Poutanen & Svensson 1996), with the disk blackbody, `diskbb`, modified by the interstellar absorption described by the model `tbabs`. This model has been used to fit the broadband spectra of many AXMPs (see, e.g., Falanga et al. 2005a, 2005b, 2011, 2012; Gierliński & Poutanen 2005; De Falco et al. 2017a, 2017b; Li et al. 2018, 2021; Kuiper et al. 2020). To account for cross-calibration uncertainties between different instruments, a multiplication factor is included in the fits. The factor is fixed at unity for NICER and set free for Insight-HXMT ME/HE. The main parameters are the Thomson optical depth across the slab, $\tau_{\rm T}$, the electron temperature, $kT_{\rm e}$, the temperature of the soft seed photons, $kT_{\rm bb}$, the normalization factor for the seed blackbody photons, $K_{\rm bb} = (R_{\rm km}/d_{10})^2$ (with d_{10} being the distance in units of 10 kpc), and the inclination angle θ (fixed at 60°) between the slab normal and the line of sight to the observer for the `compps` model; the disk temperature, $kT_{\rm diskbb}$, and normalization for the multiblackbody model; and the hydrogen column density, $N_{\rm H}$. Most of the NICER spectra showed emission lines around ∼1.6 and ∼6.5 keV, therefore we added two Gaussian components to account for these. The full model is `tbabs (Gaussian+Gaussian+diskbb +compps)` in XSPEC. The ∼1.6 keV component could have

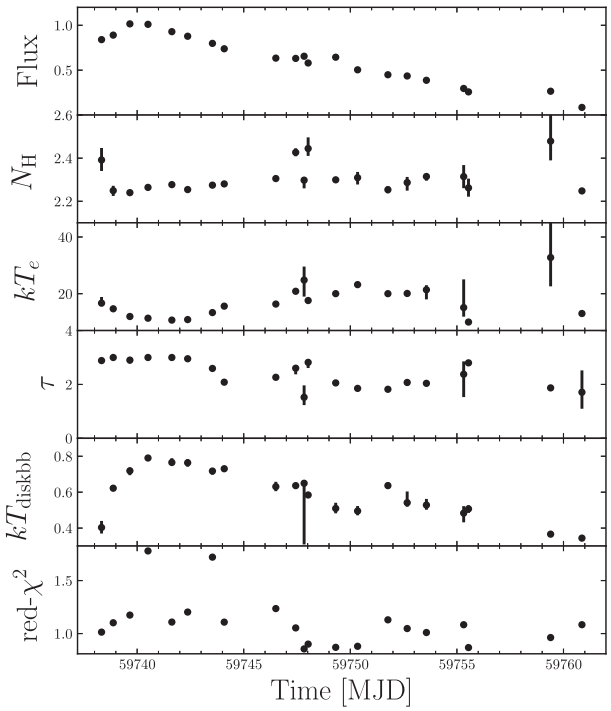

Figure 5. The fitted results of joint NICER and Insight-HXMT spectra by the model `constant×tbabs (Gaussian + Gaussian + diskbb + compps)`. From top to bottom, the bolometric flux (in units of 10^{-8} erg cm^{-2} s^{-1}), the hydrogen column density (in 10^{22} cm^{-2}), the electron temperature (in keV), the optical depth, the temperature of the disk blackbody (in keV), and the reduced χ^2 are shown.

an instrumental origin, while the ∼6.5 keV Gaussian component may come from the iron Kα line emission.

The fitted parameters are shown in Figure 5. Most of the spectra can be well fitted with reduced $\chi^2 < 1.3$. For two observations, the reduced χ^2 are larger than 1.5, which show no features in the NICER residuals and are possibly caused by the spectral evolution during the long exposures. We calculated the unabsorbed bolometric flux in the 1–250 keV range by using the tool `cflux`. During the outburst, the disk blackbody temperature increased from 0.4 to 0.8 keV in the first few days and then dropped back to ∼0.4 keV. The hydrogen column density did not change much, and the mean value is $(2.31 \pm 0.07) \times 10^{22}$ cm^{-2}. The optical depth was in the range 1.7–3.0, which explains the visibility of the hard X-ray emissions during the whole outburst. The electron temperature was around 10–25 keV. The bolometric flux reached a peak value of 1.02×10^{-8} erg cm^{-2} s^{-1} during the first few days, and in the next 20 days it decayed to 8.5×10^{-10} erg cm^{-2} s^{-1} at MJD 59760.9.

We also replaced the `compps` component by a cutoff power-law model. This model provided compatible results compared with the `compps` model, i.e., $N_{\rm H}$, the temperature and normalization of the disk blackbody component, the χ^2, and the unabsorbed flux.

4.2. Broadband Spectra Including NuSTAR Observation

We noted that the only NuSTAR observation was carried out quasi-simultaneously with some of the NICER and Insight-HXMT observations. We fitted the spectra, including the Insight-HXMT ME and HE data between MJD 59753.46–59754.40 (obs. ID P0404275015) with a total exposure of 20.99 ks (ME) and 17.51 ks (HE), NuSTAR FPMA (29.55 ks), FPMB (29.70 ks), and NICER data starting on MJD 59753.30 (5.21 ks; obs. ID 5533011501). We kept the default energy range of 3–79 keV for NuSTAR FPMA/FPMB, and for the other instruments we used the same ranges as in Section 4.1. The multiplication factors were also included to account for the cross-calibration uncertainties between the instruments. The factor was fixed at unity for the NuSTAR FPMA and set free for the other instruments. We first fitted the spectra by using an absorbed cutoff power-law model in combination with a disk blackbody model and two additional Gaussians. The best-fitted model yielded $N_{\rm H} \approx 2.30 \times 10^{22}$ cm^{-2}, a photon index $\Gamma \approx 1.54$, a cutoff energy $E_{\rm cut} \approx 24.1$ keV, the Gaussian at 5.44 keV with a width of 1.32 keV, a disk temperature $kT_{\rm diskbb} \approx 0.61$ keV, and a reduced $\chi^2 \sim 1.15$ for a total dof of 2300. We then replaced the phenomenological cutoff power-law model by the thermal Comptonization model `compps`, which is `tbabs (Gaussian+Gaussian +diskbb+compps)`. We obtained a best-fit reduced χ^2 of 1.17. We noticed that a reflection feature has been reported by Chauhan et al. (2022), therefore the reflection parameter, R, of `compps` was set free. The best-fit reduced χ^2 decreased to 1.11 for a total dof of 2298, better than the cutoff power-law model. The best-fit parameters are listed in Table 2 and the broadband spectrum is shown in Figure 6. The NICER spectrum contributed the most significant residuals. Considering such a large data set, this model provides an acceptable fit to the spectra. We obtained a normalization factor for the seed photons, $K_{\rm bb} = 65.9 \pm 6.8$, which implies a size of blackbody emitting region $R_{\rm bb} = 0.34\sqrt{K_{\rm bb}} \approx 3$ km for a distance of 3.4 kpc (Wang et al. 2023, submitted; see also Chen et al. 2022). This region is smaller than the whole NS surface with a typical radius of 12 km. However, the true emitting size should be larger, since part of the photons were reflected by the accretion disk. It is worthy to note that it is difficult to constrain the reflection contribution by only using the joint NICER and Insight-HXMT/ME/HE spectra, i.e., without NuSTAR data, the χ^2_r is 1.0; see Section 4.1.

We also changed the `compps` model to a relativistic reflection model, `relxillCp` (Dauser et al. 2016), in which the reflection spectrum is calculated using the Comptonization continuum `nthcomp`. After many attempts, during the fit, we set the iron abundance, $A_{\rm Fe}$, the density of the accretion disk, $\log N$, the ionization parameter, $\log \xi$, the power-law index of the incident spectrum, Γ, the reflection fraction, R_f, and the outer emissivity index, q_2, free to vary. The spin parameter was fixed at 0.248 for the NS spin frequency of 528 Hz. The outer disk radius was fixed at $1000\,R_{\rm ISCO}$. The inclination angle, i, was also fixed at 60°. Other parameters were fixed at their default values. This model gave a best-fit reduced χ^2 of 1.11 for a total dof of 2295, slightly larger than the `compps` model. The results are listed in Table 2.

5. Summary and Discussion

In this paper, we have reported on detailed timing and spectral analyses of Insight-HXMT, NICER, and NuSTAR data collected from the newly confirmed AMXP MAXI J1816−195 during its 2022 outburst. The outburst of MAXI J1816−195 reached its peak flux within the first few days at $\sim 1 \times 10^{-8}$ erg cm^{-2} s^{-1} and decayed into a quiescent state in the next ∼25 days. The outburst profile observed from MAXI J1816−195 is quite similar to those of other AMXPs,

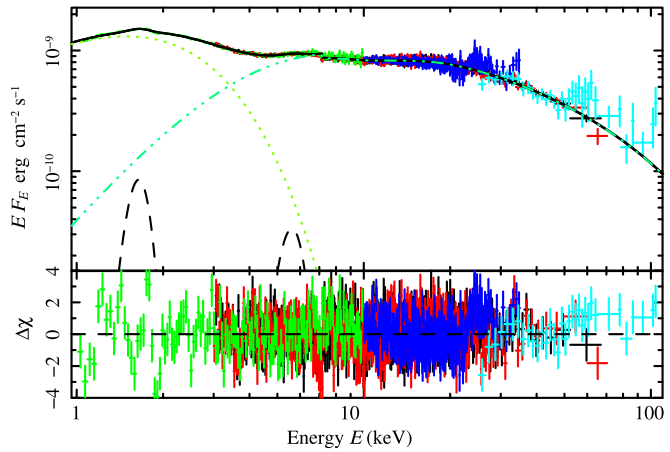

Figure 6. The unabsorbed spectra of MAXI J1816−195 from NICER, NuSTAR FPMA, NuSTAR FPMB, Insight-HXMT ME, and Insight-HXMT HE in the 1–150 keV energy range. The fitting model is `constant×tbabs (Gaussian+Gaussian+diskbb+compps)`. The black dashed lines represent the two Gaussian lines. The best-fit model is plotted as black solid line. The disk blackbody and `compps` components are shown in dotted and dashed–dotted–dotted–dotted lines, respectively.

Table 2
The Spectral Fitting to the Broadband Spectra of MAXI J1816−195 with the NICER/NuSTAR/Insight-HXMT Observations

Parameter (Units)	Best-fit Values	
$N_{\rm H}$ (10^{22} cm^{-2})	2.25 ± 0.01	2.41 ± 0.01
$E_{\rm line,1}$ (keV)	1.62 ± 0.02	1.66 ± 0.02
σ_1 (keV)	0.13 ± 0.01	0.09 ± 0.01
Norm$_1$($\times 10^{-3}$)	6.5 ± 0.6	4.2 ± 0.7
$E_{\rm line,2}$ (keV)	5.53 ± 0.06	5.78 ± 0.05
σ_2 (keV)	0.48 ± 0.07	0.76 ± 0.06
Norm$_2$($\times 10^{-4}$)	8 ± 2	26 ± 4
Inclination (deg)	60 (fixed)	60 (fixed)
$kT_{\rm diskbb}$ (keV)	0.63 ± 0.01	0.55 ± 0.01
$K_{\rm diskbb}$ (km^2)	770 ± 38	826 ± 58
$kT_{\rm e}$ (keV)	35.6 ± 1.1	16.8 ± 0.6
q_2	⋯	1.87 ± 0.49
Γ	⋯	1.88 ± 0.01
$\log \xi$	⋯	4.31 ± 0.1
$\log N$	⋯	17.98 ± 0.38
$kT_{\rm bb,seed}$ (keV)	1.31 ± 0.03	⋯
$\tau_{\rm T}$	0.89 ± 0.04	⋯
R	1.34 ± 0.09	6.51 ± 4.67
Norm$_{\rm refl.}$ ($\times 10^{-4}$)	⋯	8.3 ± 1.2
$K_{\rm compps}$ (km^2)	65.0 ± 6.8	⋯
$C_{\rm NuSTAR/FPMA}$	1 (fixed)	1 (fixed)
$C_{\rm NuSTAR/FPMB}$	1.01 ± 0.01	1.01 ± 0.01
$C_{\rm NICER}$	1.05 ± 0.01	1.05 ± 0.01
$C_{\rm Insight-HXMT/ME}$	1.11 ± 0.01	1.11 ± 0.01
$C_{\rm Insight-HXMT/HE}$	1.20 ± 0.03	1.21 ± 0.05
χ^2/d. o. f.	2543.6/2298	2550.9/2295
$F_{\rm bol}$ (10^{-9} erg s^{-1} cm^{-2})[a]	3.97 ± 0.01	3.96 ± 0.01

Notes. Best-fit parameters determined from the fits to the average broadband spectrum of MAXI J1816−195 performed with the NICER/NuSTAR/Insight-HXMT data. The multiplication factors for all instruments are provided. The best-fit results in the middle and right columns are from the models `constant×tbabs (Gaussian+Gaussian+diskbb+compps)` and `constant×tbabs (Gaussian+Gaussian+diskbb+relxillCp)`, respectively.
[a] Unabsorbed flux in the 1–250 keV energy range.

showing a fast rise (∼1–2 days) and an exponential followed by a linear decay, which can be explained by the disk instability model (King & Ritter 1998; Powell et al. 2007).

During the full outburst, hard X-ray/soft γ-ray emission was detected up to ∼200 keV. The joint NICER and Insight-HXMT spectra in the energy of 1–150 keV were well fitted by a combination of a multicolor disk blackbody and Comptonization model `compps`, with two additional Gaussian lines, exposed to interstellar extinction. A joint spectral fit including quasi-simultaneous NuSTAR, NICER, and Insight-HXMT ME/HE data showed emission reflected from the accretion disk, which can be modeled by the reflected `compps` model or the `relxillCP` model.

Usually, the hard X-ray emission from AMXPs is relatively weak and typically has pulsation amplitudes of less than 10% (see, e.g., Papitto et al. 2020 and references therein; see also Falanga et al. 2005b for IGR J00291+5934 with a pulsed fraction of ∼12%–20% at ∼100 keV). Therefore, the pulsations of most AMXPs are mostly detected at soft X-rays with the instruments on board, e.g., RXTE, XMM-Newton, or NICER. At hard X-rays, Insight-HXMT observed Swift J1756.9–2508 during its 2018 outburst and detected the X-ray pulsations up to ∼100 keV using an ephemeris determined by NICER at soft X-rays (Li et al. 2021). In the case of MAXI J1816−195, at hard X-rays both the ME and HE on board Insight-HXMT were capable of deriving the pulsar ephemeris directly from their event data, obtaining parameters well consistent with those derived by NICER at soft X-rays. In particular, our timing analysis using the DE405 solar system ephemeris and the most accurate VLA (Beauchamp et al. 2022) source location for MAXI J1816−195 in the barycentering process, contrary to Bult et al. (2022a), who used DE430 and the less accurate (∼0.″4 difference) Swift location (Kennea et al. 2022), yielded consistent orbital and spin parameters with Bult et al. (2022a) at 1σ confidence.

From Insight-HXMT observations, hard X-ray pulsations have been detected significantly up to ∼95 keV. The pulse profiles in the 0.8–95 keV band are well described by a truncated Fourier series. The phase angles of the fundamental and the first overtone are nearly constant for energies below ∼60 keV, implying that most photons are likely emitted from the same region at the NS surface with a very similar emission pattern. The observed pulse profiles could be used to measure the NS mass and radius (Poutanen & Gierliński 2003) of MAXI J1816−195 in a future study.

The stability of the pulse profiles across a broad energy range allows us to determine the absolute timing accuracy of Insight-HXMT in detail. Cross-correlating Insight-HXMT ME and NICER pulse profiles for the overlapping 5–10 keV energy band yielded a phase shift $\delta\Phi$ of only -0.008 ± 0.005, consistent with zero, suggesting that both instruments are well aligned within 14 μs, with the Insight-HXMT ME events arriving a little bit later than NICER ones. A similar correlation analysis between Insight-HXMT ME and HE pulse profiles for the 20–35 keV band resulted in a difference of only 0.9 μs, with an uncertainty of 13.9 μs.

Bult et al. (2022a) performed a coherent timing analysis adopting a constant frequency and a flux bias model using NICER ToAs covering the *full* outburst period. They found unacceptably high χ^2 values for both models, assumptions resulting in complex timing residuals for the first four to five days during the rising part of the outburst, a flat shape during

the next ∼20 days in the decay phase, and, finally, (linearly) increasing phase deviations at the end of the outburst, also visible at the very beginning of the outburst.

In this work, we have analyzed the timing data from Insight-HXMT ME and HE observations as well as from NICER and found that the ToAs from the different (independent) instruments were well consistent with each other in spite of their different bandpass. The timing residuals showed erratic behavior (or a V-shaped wedge) during the rising part of the outburst between MJD 59737.0 and 59741.9, similar to the results shown in Bult et al. (2022a).

For the decaying part of the outburst between MJD 59741.9–59760.6, we detected a significant positive quadratic term $\dot{\nu}$ of $(9.0 \pm 2.1) \times 10^{-14}$ Hz s^{-1} fitting a two-parameter timing model, including ν and $\dot{\nu}$, yielding an acceptable χ^2, which could interpreted as a spinup.

We realize that such spinup or spindown terms can arise when an inaccurate source location is used in the barycentering process. However, in our work, we have used the subarcsecond-accurate VLA location for MAXI J1816−195, with an accuracy better than 0.″005. This uncertainty on the location can account for an uncertainty in the spinup rate (see e.g., Sanna et al. 2020 for the formulae) of only $\sim 2.0 \times 10^{-16}$ Hz s^{-1}, 2.7 orders of magnitude smaller than the measured $\dot{\nu}$ value and much smaller than our error estimate of 2.1×10^{-14} Hz s^{-1}. On the contrary, if we should have used the Swift-XRT location in the barycentering process, with a centroid 0.″4 from the VLA location and an estimated error radius of 2.″2, then the uncertainty in the quadratic term would be ∼80 times larger, i.e., of the order of 1.6×10^{-14} Hz s^{-1}, comparable to our measurement error. Therefore, we assume that the measured value for $\dot{\nu}$ during the decay phase is accurate and genuine, and could be interpreted as a gain of angular momentum by the NS from the accreted matter.

During the outburst, X-ray pulsations have been detected at bolometric flux states with a flux between $\sim(0.1 \text{ and } 1) \times 10^{-8}$ erg cm^{-2} s^{-1}. Adopting a source distance of 3.4 kpc, as constrained by Wang et al. (2023, submitted; see also Chen et al. 2022), these bolometric fluxes correspond to accretion rates in the range $(0.012\text{–}0.12)\dot{M}_{\rm Edd}$, where $\dot{M}_{\rm Edd} = 2 \times 10^{-8} M_{\odot}$ yr^{-1} is the Eddington rate, assuming that $L = \eta \dot{M} c^2$ and a typical value of $\eta = 0.1$ for NS (Frank et al. 2002). By adopting Equations (11) and (12) and the same assumptions in Psaltis & Chakrabarty (1999), these limits allow us to constrain the surface dipole magnetic field strength of $(0.25\text{–}74) \times 10^8$ G (see also Hartman et al. 2008). If 20% uncertainty of distance is considered, the magnetic field is in the range of $(0.2\text{–}85) \times 10^8$ G. The possible bolometric correction factor of the flux would not change the magnetic field significantly, because the measured fluxes are covered by a broadband energy range.

During the spinup period, the averaged bolometric flux is 0.56×10^{-8} erg cm^{-2} s^{-1}, corresponding to $0.065\dot{M}_{\rm Edd}$. If the spinup of the pulsar is solely induced by the angular momentum transferred from the accreted material to the NS, the magnetic field can be determined from the relation (Shapiro & Teukolsky 1983; Tong 2015; Pan et al. 2022)

$$B = 0.1 I_{45}^{7/2} R_6^{-3} M_{1.4}^{-3/2} \dot{\nu}_{-13}^{7/2} \left(\frac{\dot{M}}{0.065 \dot{M}_{\rm Edd}} \right)^{-3} \times 10^8 \text{ G}, \quad (2)$$

where I_{45}, R_6, $M_{1.4}$, and $\dot{\nu}_{-13}$ are the moment of inertia, the NS radius and mass, and the spinup, in units of 10^{45} g cm^2, 10^6 cm, $1.4 M_{\odot}$, and 10^{-13} Hz s^{-1}, respectively. By adopting $I_{45} = 1.5$ (see, e.g., Worley et al. 2008) and the measured spinup rate, we obtain a magnetic field strength of $(0.04\text{–}2) \times 10^8$ G. Combined with the aforementioned range, the magnetic field strength of MAXI J1816−195 is $(0.2\text{–}2) \times 10^8$ G, which is comparable with the magnetic field strengths estimated for several other AMXPs (see, e.g., Hartman et al. 2008, 2009, 2011; Patruno et al. 2009; Patruno 2010; Papitto et al. 2011).

Acknowledgments

We appreciate the referee for all the valuable comments and suggestions that led to the improvement of the manuscript. This work was supported by the Major Science and Technology Program of Xinjiang Uygur Autonomous Region (No. 2022A03013-3). Z.S.L., Y.Y.P., and L.J. were supported by the National Natural Science Foundation of China (grant Nos. 12103042, U1938107, 12273030, and 12173103). S.Z. is supported by the National Key R&D Program of China (2021YFA0718500). J.P. acknowledges support from the Academy of Finland, grant No. 333112. This work is also supported by the International Partnership Program of the Chinese Academy of Sciences (grant No. 113111KYSB20190020). This work has made use of data from the Insight-HXMT mission, a project funded by the China National Space Administration (CNSA) and the Chinese Academy of Sciences (CAS), and also from the High Energy Astrophysics Science Archive Research Center (HEASARC), provided by NASA's Goddard Space Flight Center.

Facilities: Insight-HXMT, NICER, NuSTAR.

ORCID iDs

Zhaosheng Li https://orcid.org/0000-0003-2310-8105
Lucien Kuiper https://orcid.org/0000-0002-7889-6586
Mingyu Ge https://orcid.org/0000-0002-3776-4536
Maurizio Falanga https://orcid.org/0000-0003-3095-6065
Juri Poutanen https://orcid.org/0000-0002-0983-0049
Long Ji https://orcid.org/0000-0001-9599-7285
Renxin Xu https://orcid.org/0000-0002-9042-3044
Liming Song https://orcid.org/0000-0003-0274-3396
Jinlu Qu https://orcid.org/0000-0002-9796-2585
Fangjun Lu https://orcid.org/0000-0003-3248-6087
Shuang-Nan Zhang https://orcid.org/0000-0001-5586-1017

References

Alpar, M. A., Cheng, A. F., Ruderman, M. A., & Shaham, J. 1982, Natur, 300, 728
Arnaud, K. A. 1996, in ASP Conf. Ser. 101, Astronomical Data Analysis Software and Systems V, ed. G. H. Jacoby & J. Barnes (San Francisco, CA: ASP), 17
Bachetti, M., Markwardt, C. B., Grefenstette, B. W., et al. 2021, ApJ, 908, 184
Beardmore, A. P., Kennea, J. A. & Swift/XRT Team 2022, ATel, 15506, 1
Beauchamp, I., Belvedere, S., Hernandez, M., et al. 2022, ATel, 15481, 1
Bright, J., Russell, T., Tremou, E., et al. 2022, ATel, 15484, 1
Buccheri, R., Bennett, K., Bignami, G. F., et al. 1983, A&A, 128, 245
Bult, P., Altamirano, D., Arzoumanian, Z., et al. 2022a, ApJL, 935, L32
Bult, P. M., Ng, M., Altamirano, W. I. D., et al. 2022b, ATel, 15425, 1
Bult, P. M., Sanna, A., Ng, M., et al. 2022c, ATel, 15431, 1
Campana, S., & Di Salvo, T. 2018, in The Physics and Astrophysics of Neutron Stars (Astrophysics and Space Science Library) Vol. 457ed. L. Rezzolla et al. (Berlin: Springer), 149
Cao, X., Jiang, W., Meng, B., et al. 2020, SCPMA, 63, 249504
Cavecchi, Y., Galloway, D. K., Goodwin, A. J., Johnston, Z., & Heger, A. 2020, MNRAS, 499, 2148
Chauhan, J., Lohfink, A., Bharali, P., et al. 2022, ATel, 15470, 1

Chen, Y., Cui, W., Li, W., et al. 2020, SCPMA, 63, 249505
Chen, Y.-P., Zhang, S., Ji, L., et al. 2022, ApJL, 936, L21
Dauser, T., García, J., Walton, D. J., et al. 2016, A&A, 590, A76
De Falco, V., Kuiper, L., Bozzo, E., et al. 2017a, A&A, 603, A16
De Falco, V., Kuiper, L., Bozzo, E., et al. 2017b, A&A, 599, A88
de Martino, D., D'Avanzo, P., Ambrosino, F., et al. 2022, ATel, 15479, 1
Di Salvo, T., & Sanna, A. 2022, in Millisecond Pulsars, ed. S. Bhattacharyya, A. Papitto, & D. Bhattacharya (Cham: Springer), 87
Falanga, M., Bonnet-Bidaud, J. M., Poutanen, J., et al. 2005a, A&A, 436, 647
Falanga, M., Kuiper, L., Poutanen, J., et al. 2005b, A&A, 444, 15
Falanga, M., Kuiper, L., Poutanen, J., et al. 2011, A&A, 529, A68
Falanga, M., Kuiper, L., Poutanen, J., et al. 2012, A&A, 545, A26
Frank, J., King, A., & Raine, D. J. 2002, Accretion Power in Astrophysics (3rd edn.; Cambridge: Cambridge Univ. Press), 398
Gierliński, M., & Poutanen, J. 2005, MNRAS, 359, 1261
Hartman, J. M., Galloway, D. K., & Chakrabarty, D. 2011, ApJ, 726, 26
Hartman, J. M., Patruno, A., Chakrabarty, D., et al. 2008, ApJ, 675, 1468
Hartman, J. M., Patruno, A., Chakrabarty, D., et al. 2009, ApJ, 702, 1673
Kaastra, J. S., & Bleeker, J. A. M. 2016, A&A, 587, A151
Kennea, J. A., Evans, P. A., & Negoro, H. 2022, ATel, 15421, 1
King, A. R., & Ritter, H. 1998, MNRAS, 293, L42
Kong, A. K. H. 2022, ATel, 15501, 1
Kuiper, L., & Hermsen, W. 2009, A&A, 501, 1031
Kuiper, L., Tsygankov, S. S., Falanga, M., et al. 2020, A&A, 641, A37
Li, Z., De Falco, V., Falanga, M., et al. 2018, A&A, 620, A114
Li, Z., Kuiper, L., Falanga, M., et al. 2022, ATel, 15471, 1
Li, Z. S., Kuiper, L., Falanga, M., et al. 2021, A&A, 649, A76
Liu, C., Zhang, Y., Li, X., et al. 2020, SCPMA, 63, 249503
Mandal, M., Pal, S., Chauhan, J., Lohfink, A., & Bharali, P. 2023, MNRAS, 521, 881
Negoro, H., Serino, M., Iwakiri, W., et al. 2022, ATel, 15418, 1
Pan, Y. Y., Li, Z. S., Zhang, C. M., & Zhong, J. X. 2022, MNRAS, 513, 6219
Papitto, A., Falanga, M., Hermsen, W., et al. 2020, NewAR, 91, 101544
Papitto, A., Ferrigno, C., Bozzo, E., et al. 2013, Natur, 501, 517
Papitto, A., Riggio, A., Burderi, L., et al. 2011, A&A, 528, A55
Patruno, A. 2010, ApJ, 722, 909
Patruno, A., Altamirano, D., Hessels, J. W. T., et al. 2009, ApJ, 690, 1856
Patruno, A., & Watts, A. L. 2021, in Timing Neutron Stars: Pulsations, Oscillations and Explosions (Astrophysics and Space Science Library, Vol. 461) ed. T. M. Belloni, M. Méndez, & C. Zhang (Berlin: Springer), 143
Poutanen, J., & Gierliński, M. 2003, MNRAS, 343, 1301
Poutanen, J., & Svensson, R. 1996, ApJ, 470, 249
Powell, C. R., Haswell, C. A., & Falanga, M. 2007, MNRAS, 374, 466
Psaltis, D., & Chakrabarty, D. 1999, ApJ, 521, 332
Radhakrishnan, V., & Srinivasan, G. 1982, CSci, 51, 1096
Remillard, R. A., Loewenstein, M., Steiner, J. F., et al. 2022, AJ, 163, 130
Sanna, A., Burderi, L., Gendreau, K. C., et al. 2020, MNRAS, 495, 1641
Shapiro, S. L., & Teukolsky, S. A. 1983, Black Holes, White Dwarfs, and Neutron Stars: the Physics of Compact Objects (New York: Wiley)
Tong, H. 2015, RAA, 15, 517
Wijnands, R., & van der Klis, M. 1998, Natur, 394, 344
Worley, A., Krastev, P. G., & Li, B.-A. 2008, ApJ, 685, 390
Zhang, S.-N., Li, T., Lu, F., et al. 2020, SCPMA, 63, 249502